PERIODICO di MINERALOGIA
established in 1930

DIPARTIMENTO DI SCIENZE DELLA TERRA
SAPIENZA UNIVERSITÀ DI ROMA

An International Journal of
Mineralogy, Crystallography, Geochemistry,
Ore Deposits, Petrology, Volcanology
and applied topics on Environment, Archaeometry and Cultural Heritage

Thermal behavior of schorl up to breakdown temperature at room pressure

Paolo Ballirano [1], Beatrice Celata [1,*], Ferdinando Bosi [1], Christopher E. Beckett-Brown [2], Giovanni B. Andreozzi [1]

[1] Department of Earth Sciences, Sapienza University of Rome, Piazzale Aldo Moro, 5-I-00185 Roma, Italy
[2] Geological Survey of Canada, Ottawa, Ontario K1A 0E8, Canada

ARTICLE INFO

Submitted: September 2022
Accepted: January 2023
Available on line: January 2023

* Corresponding author:
beatrice.celata@uniroma1.it

Doi: 10.13133/2239-1002/17859

How to cite this article:
Ballirano P. et al. (2023)
Period. Mineral. 92, 23-32

ABSTRACT

Schorl is one of the most widespread tourmaline compositions in the world, known from many different geological settings. Its role as boron and water carrier has been moderately investigated together with its stability field. In this study, the richest schorl in Fe^{2+} content was investigated to constraint its breakdown temperature at room pressure through *in situ* powder X-Ray Diffraction (*in situ* pXRD), its breakdown products and the coupled thermally induced dehydrogenation-dehydrogenation process experienced approaching the breakdown conditions.

Schorl turned out to begin its breakdown at 850 °C with the first appearance of hematite, followed by a dominant B-mullite phase. The breakdown reaction of schorl can be expressed as follows: $2NaFe^{2+}{}_3Al_6(BO_3)_3Si_6O_{18}(OH)=3Fe_2O_3+4/3Al_9Si_2BO_{19}$+(Na- Si-B-rich) glass+$4H_2O$.

The breakdown process is completed at 950 °C, when no trace of residual tourmaline is found. Annealing the schorl at 450 °C in air was enough to set the Fe oxidation out, counterbalanced by the deprotonation reaction: $(Fe^{2+})+(OH)^- \rightarrow (Fe^{3+})+(O^{2-})+1/2H_2(g)$.

Keywords: Schorl; HT-pXRD; thermal expansion; iron oxidation; deprotonation; intracrystalline cations exchange; structural breakdown.

INTRODUCTION

Tourmalines are classified as a supergroup of complex borosilicates, being the dominant boron minerals commonly found as accessory phases in sedimentary, metamorphic, and igneous rocks.

Their ubiquity is given by different factors: the capacity to accommodate a variety of chemical elements in their crystal structure, so as to adapt to different geological environments, and the features of their crystal structure itself hence their mechanical resistance.

The general formula for tourmaline supergroup minerals is: $XY_3Z_6T_6O_{18}(BO_3)_3V_3W$, where X=$Na^+$, K^+, Ca^{2+}, □ (= vacancy); Y=Al^{3+}, Fe^{3+}, Cr^{3+}, V^{3+}, Mg^{2+}, Fe^{2+}, Mn^{2+}, Li^+; Z = Al^{3+}, Fe^{3+}, Cr^{3+}, V^{3+}, Mg^{2+}, Fe^{2+}; T=Si^{4+}, Al^{3+}, B^{3+}; B = B^{3+}; V=$(OH)^-$, O^{2-}; W = $(OH)^-$, F^-, O^{2-}. The unitalicized letters X, Y, Z, T and B represent groups of cations at the $^{[9]}X$, $^{[6]}Y$, $^{[6]}Z$, $^{[4]}T$ and $^{[3]}B$ crystallographic sites (italicized letters), whereas the letters V and W represent groups of anions accommodated at the [3]-coordinated O3 and O1 crystallographic sites, respectively. Tourmaline-supergroup minerals are primarily classified into three groups, vacant, alkali and calcic, based on the *X*-site occupancy (Henry et al., 2011). A further level of classification into subgroups is based on charge arrangements at the *Y* and *Z* sites. Tourmalines are also distinguished by the dominant anion at the W position of the general formula into hydroxy-,

fluor- and oxy-species. A more comprehensive discussion on tourmaline crystal-chemistry is given in Bosi (2018).

Depending on its composition, tourmaline appeared to be stable at different pressure and temperature conditions: a preliminary diagram of the extensive tourmaline's stability field was provided by van Hinsberg et al. (2011). Most of the experimental work done to investigate the boundaries of tourmaline's stability field was carried out on dravite or schorl (which are the most widespread compositions), considered in an artificial multi-phase system (Robbins and Yoder, 1962; Holtz and Johannes, 1991; Ota et al., 2008). Pure tourmaline systems with samples of dravitic and schorlitic composition were investigated at High Temperature (H*T*) and Room Pressure (R*P*) by Pieczka and Kraczka (2004), Bačik et al. (2011), Liu et al. (2019), Hovis et al. (2022). The present work aims at constraining the breakdown temperature of a natural schorl, ideally $NaFe^{2+}{}_3Al_6(Si_6O_{18})(BO_3)_3(OH)_3(OH)$, as reported by Andreozzi et al. (2020), in a mono-phase system through *in situ* High-Temperature powder X-Ray Diffraction (HT-pXRD) at room pressure, focusing on the thermally induced dehydrogenation-oxidation coupled mechanism and identifying the eventual breakdown products.

EXPERIMENTAL

A representative black Seagull schorl single crystal was selected and a small fragment was separated and gently ground under ethanol in an agate mortar. The same material was analyzed in detail by Andreozzi et al. (2020) that reported an empirical formula $^{X}(Na_{0.74}\square_{0.24}K_{0.01}Ca_{0.01})_{S1.00}{}^{Y}(Fe^{2+}{}_{2.05}Al_{0.92}Ti_{0.02}Mn_{0.01}Zn_{0.01})_{S3.00}{}^{Z}(Al_{5.41}Fe^{2+}{}_{0.53}Mg_{0.06})_{S6.00}(Si_6O_{18})(BO_3)_3{}^{V}(OH)_3{}^{W}[(OH)_{0.46}F_{0.41}O_{0.13}]$. The resulting powder was loaded in the tip of a 0.5 mm diameter SiO_2-glass capillary. A wad of kaolin wool-glass was used as a stopper to avoid movements of the powder along the capillary. The portion of the capillary filled by the powder was of ca. 25 mm in length. Subsequently, the capillary was fixed to a hollow corundum tube using a H*T* cement and aligned onto a standard goniometer head.

In situ H*T*-pXRD data were collected using a heating chamber whose description, as well as details of its thermal calibration, can be found in Ballirano and Melis (2007).

Diffraction data were measured, using Cu$K\alpha$ radiation, with a Bruker AXS D8 Advance which operates in transmission mode. The instrument is fitted with focusing multilayer graded (Göbel) mirrors along the incident beam, Soller slits on both the incident (2.3° opening angle) and diffracted (radial) beam, and with a position sensitive detector (PSD) VÅntec-1 set at an opening angle of 6° 2θ.

According to the large transition elements (TE) content of the sample, both a high absorption (calculated μR=3.18, for an estimated packing efficiency of 60%) and a significant secondary fluorescence were expected. Preliminary data collections confirmed the existence of the problem, possibly limiting the extraction of reliable structural parameters especially at H*T*. A diffraction pattern was measured at room temperature (R*T*) outside the chamber for a characterization of the sample owing to the possible chemical inhomogeneity of the crystal from which the fragment was extracted. The pattern indicated the occurrence in mixture of traces of quartz.

High-*T* data were measured in the 30-925 °C range. After reaching the maximum temperature, the capillary was cooled back at R*T* within the chamber with a 10 °C/min cooling rate. Following the procedure adopted by Celata et al. (2021) and Ballirano et al. (2022 a,b), to avoid the effect of textured recrystallization at the walls of the capillary, the powder was extracted, re-homogenized, and loaded in a new capillary for performing a data collection keeping the capillary outside the chamber.

Data were evaluated by the Rietveld method using Topas V.6 (Bruker AXS 2016). This program adopts the Fundamental Parameters Approach (FPA: Cheary and Coelho, 1992) to model the peak shape. The equation of Sabine et al. (1998) was used to correct for absorption effects of a cylindrical sample and the procedure described in Ballirano and Maras (2006) was followed to remove the correlation existing between displacement parameters and absorption. The isotropic displacement parameters were constrained as follow: $B_Y=B_Z=B=B_T$; $B_{O1}=B_{O3}$; $B_{O2}=B_{O4}=B_{O5}=B_{O6}=B_{O7}=B_{O8}$; $B_{H1}=B_{H3}=1.2 * B_{O1}$. Owing to the impossibility to refine simultaneously the site occupancy fraction (*sof*) and the displacement parameter of the *X* site, the *sof* was kept fixed at the starting value. Preferred orientation effects were modelled using spherical harmonics (8^{th}-order, nine refinable parameters: Ballirano, 2003). Starting structural data were taken from Andreozzi et al. (2020) and each refined structure at a given non-ambient *T* was used as input for the subsequent *T*. Miscellaneous data of the R*T* data collection and of the Rietveld refinement are listed in Table 1. Unit-cell parameters determined at R*T* are shown in Table 2, relevant bond distances, isotropic displacement parameters, and mean atomic number (*man*; Hawthorne et al., 1995) at R*T* are reported in Table 3. Miscellaneous data of the H*T* data collection and of the Rietveld refinements are given in Table 4. A magnified 3D-plot of the full data set is shown in Figure 1 and a representative example of Rietveld plots is shown in Figure 2. The CIF of the schorl structure refined at R*T* is given in Online Resource.

RESULTS AND DISCUSSION

RT structure of the schorl sample

The Rietveld refinement confirms the occurrence in mixture of 1.22(5) wt% of quartz (Figure S1).

The structure at R*T* is in close agreement, despite

Table 1. Miscellaneous data of the R*T* data collection and Rietveld refinement.

2θ range (°)	7-145
2θ step-size (°)	0.021798
Counting time (s)	8
Rp (%)	0.521
Rwp (%)	0.807
R_{Bragg} (%)	0.429
DWd	1.296
χ^2	1.751
Quartz (wt%)	1.22(5)

Definition of the statistical indicators as indicated in Young (1993).

Table 2. Unit-cell parameters at R*T* of the schorl sample. Data of Andreozzi et al. (2020) are reported for comparison.

	Andreozzi et al. (2020)	Present work
a (Å)	15.9957(3)	16.00573(11)
c (Å)	7.1863(2)	7.19134(6)
V (Å^3)	1592.36(7)	1595.48(3)

the relatively large standard uncertainties (ss), with that refined from single-crystal X-ray diffraction measurements (Andreozzi et al., 2020). However, the present unit-cell parameters are slightly larger than those of reference data (Table 2), suggesting some chemical differences between the two fragments as already reported by Sinclair and Richardson (1992). Moreover, refined *man* (Table 3) indicates its increase at the *Y* site in the present sample [22.93(11) *vs* 22.06(4)], whereas that at *Z*, it is similar [13.93(9) *vs* 14.14(3)] to the data of Andreozzi et al. (2020).

Bond distances are consistent with the data of Andreozzi et al. (2020) showing only minor differences. Both <*Y*-O> and <*Z*-O> are slightly shorter in the present sample (2.034 Å vs 2.051 Å and 1.914 Å vs 1.924 Å) and they nicely plot within the structural-stability limits for tourmaline minerals (Bosi and Lucchesi, 2007; Bosi, 2018; Andreozzi et al., 2020). By contrast, the observed <*X*-O> is slightly longer (2.716 Å vs 2.700 Å) than that reported by Andreozzi et al. (2020). It is worth noting that the observed differences in mean bond-distances are of the order of 2-3s of the individual bond distances, thus

Table 3. Relevant bond distances (Å), group of isotropic displacement parameters (Å^2: see text for explanation) and mean atomic number (*man*) of *Y* and *Z* sites. Data of Andreozzi et al. (2020) are reported for comparison.

	Andreozzi et al. (2020)	Present work
X B_{iso}	1.785	1.1(2)
<*Y,Z,B,T*> B_{iso}	0.541	0.79(3)
<$O_{1,3}$> B_{iso}	1.864	2.08(18)
<$O_{2,4\text{-}8}$> B_{iso}	0.766	0.65(6)
man Y	22.06(4)	22.93(11)
man Z	14.14(3)	13.93(9)
B-O(2)	1.366(2)	1.378(18)
B-O(8) x2	1.3807(13)	1.373(8)
<*B*-O>	1.376	1.375
T-O(6)	1.6063(9)	1.610(5)
T-O(7)	1.6093(8)	1.629(5)
T-O(4)	1.6267(5)	1.621(4)
T-O(5)	1.6397(5)	1.598(4)
<*T*-O>	1.621	1.615
X-O(2) x3	2.514(2)	2.565(10)
X-O(5) x3	2.7635(15)	2.782(9)
X-O(4) x3	2.8210(15)	2.801(9)
<*X*-O>	2.700	2.716
Y-O(2) x2	2.0020(8)	2.015(5)
Y-O(6) x2	2.0414(9)	2.024(6)
Y-O(1)	2.0640(15)	2.048(7)
Y-O(3)	2.1546(15)	2.075(9)
<*Y*-O>	2.051	2.034
Z-O(6)	1.8753(9)	1.871(5)
Z-O(7)	1.8901(8)	1.879(6)
Z-O(8)	1.8910(9)	1.897(6)
Z-O(8)	1.9326(9)	1.908(7)
Z-O(7)	1.9710(9)	1.965(6)
Z-O(3)	1.9819(6)	1.961(4)
<*Z*-O>	1.924	1.914

Table 4. Miscellaneous data of the H*T* data collection and Rietveld refinements.

2θ range (°)	7-135
2θ Step-size (°)	0.021798
Counting time (s)	4
T_{max} (°C)	925
T steps (°C)	25
Heating rate (°C/min)	0.5
Rp (%)	0.878-1.014
Rwp (%)	1.172-1.243
R_{Bragg} (%)	0.385-0.548
DWd	1.131-1.730
χ^2	1.090-1.389

they may be considered as questionable. For this reason, we did not attempt to correlate variation of *man* and mean bond distances to discuss modifications of the present *Y* and *Z* site populations.

Breakdown products of schorl

The first evidence of schorl structural breakdown was observed at 850 °C owing to the occurrence of weak extra diffraction reflections (Figure 1). These reflections progressively increased in intensity at the expenses of those of schorl. The breakdown was completed at 925 °C as signaled by the complete disappearance of the schorl reflections. The diffraction pattern of the sample cooled down at R*T* (Figure 3) was used for identifying the schorl breakdown products and the pattern was refined by the Rietveld method constraining all structural parameters to reference data, except for the unit-cell parameters. Consequently, the resulting quantitative phase analysis (QPA) must be considered as semi-quantitative. Data indicate the occurrence of prevailing B-mullite and hematite as schorl breakdown products plus some amorphous material (Table 5). The occurrence of relicts of unreacted schorl results from the re-homogenisation of the powder. In fact, this procedure admixed powders coming not only from the portion bathed by the X-rays but also from inner zones of the capillary affected by some thermal gradient.

All these crystalline phases were also identified in the H*T* diffraction patterns collected at *T* 800 °C, therefore, clearly indicating that they were not produced during the cooling process. The observed assemblage of phases is similar to that observed for both Fe-rich fluor-elbaite (Celata et al., 2021) and Mn-bearing fluor-elbaite (Ballirano et al., 2022a) but is significantly different with respect to that resulting from the thermal breakdown of uvite (Ballirano et al., 2022b). In fact, the B-mullite-like phase reported as the prevailing crystalline product of the breakdown of schorl, Fe-rich fluor-elbaite, and Mn-bearing fluor-elbaite, in uvite did not form and indialite was instead observed as the dominant breakdown product.

Evaluation of the unit-cell parameters of B-mullite (Table 5) provided interesting crystal-chemical and structural information. Unit-cell parameters of B-mullite are similar to those of the product of the thermal breakdown of Fe-rich fluor-elbaite (Celata et al., 2021), whereas they are larger than those of the equivalent phase arising from the breakdown of Mn-bearing fluor-elbaite (Ballirano et al., 2022a) (Table S1). In this regard, it is worth noting that Lührs et al. (2014) have shown the existence of relations linking unit-cell parameters and B_2O_3 mol% content of B-mullites. Generally speaking, an increase of the B_2O_3 mol% content produces a progressive contraction of the

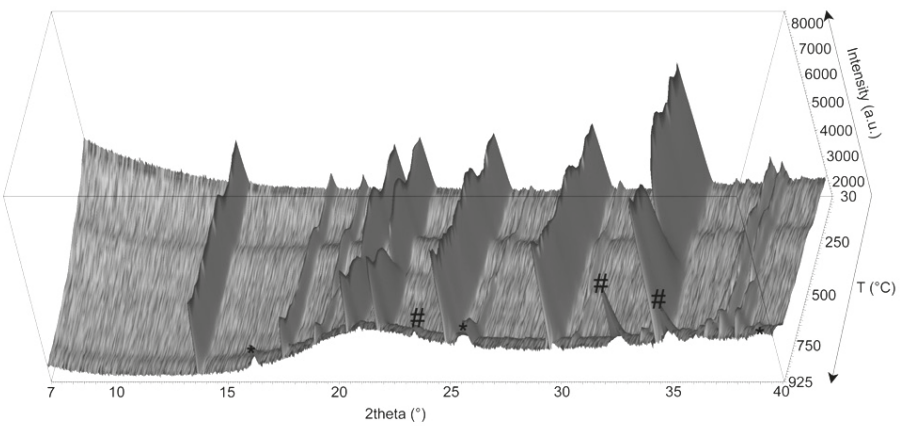

Figure 1. Magnified view (7-40° 2θ) of the full data set of the heating cycle of schorl.
* relevant reflections of hematite;# relevant reflections of B-mullite.

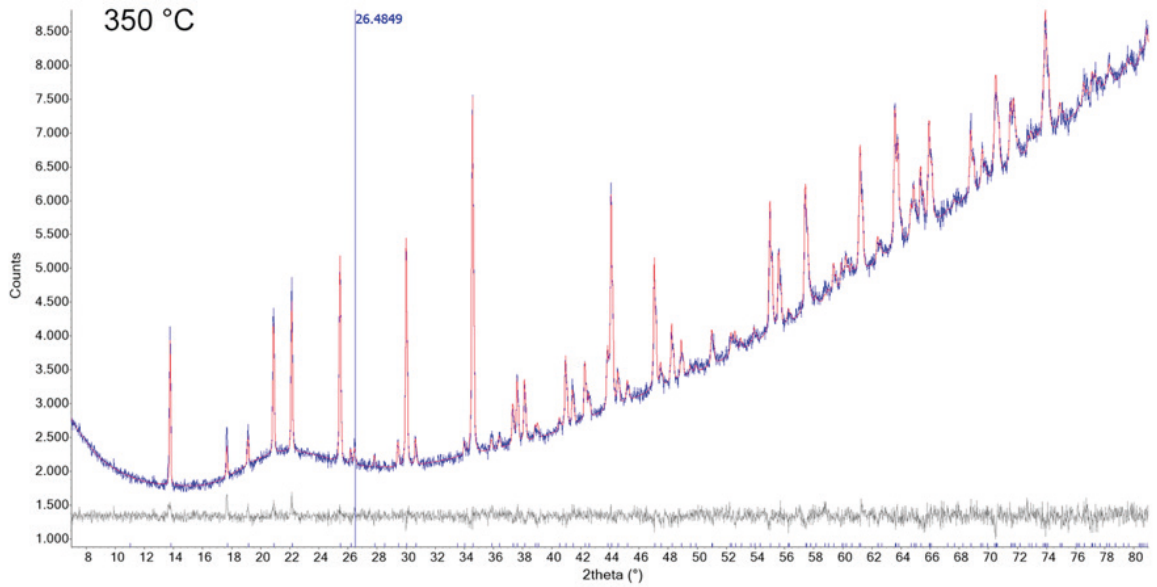

Figure 2. Magnified 7-80° 2θ view of a representative example of the Rietveld plots of the diffraction pattern collected at 350 °C. Blue: experimental; red: calculated; grey: difference; below: vertical bars indicate the position of calculated Bragg reflections of schorl. The vertical blue line identifies the position of the strongest reflection of quartz.

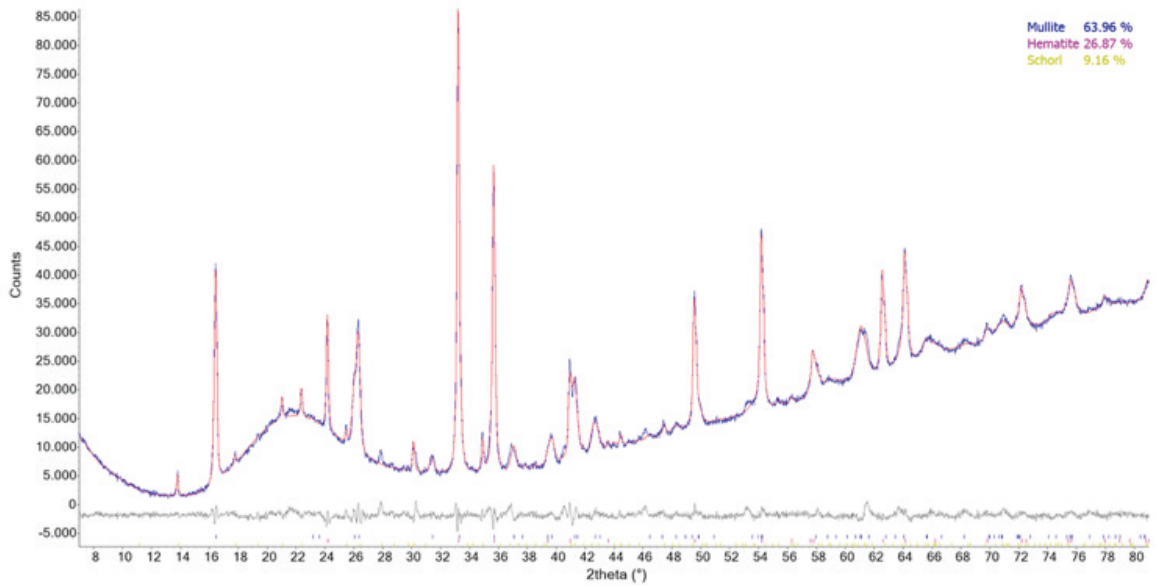

Figure 3. Magnified 7-80° 2θ view of the Rietveld plots of the products of breakdown of the schorl. Data collected at RT. Blue: experimental; red: calculated; grey: difference; vertical bars: position of calculated Bragg reflections of (from above to below) B-mullite, hematite, and schorl (unreacted). Intensities on logarithmic scale.

unit-cell values. Accordingly, in the case of the B-mullite arising from the thermal breakdown of both schorl and Fe-rich fluor-elbaite, the B_2O_3 content may be estimated, by using the various regression equations of Lührs et al. (2014), to ca. 10 mol%, whereas it is significantly higher for the B-mullite arising from the breakdown of Mn-bearing fluor-elbaite (16-17 mol%: Ballirano et al., 2022a). The different B_2O_3 mol% of the B-mullites reflects the different B_2O_3 content of the pristine tourmalines. In fact, Mn-bearing fluor-elbaite contains 0.40 additional B

Table 5. R*T* unit-cell parameters and quantitative phase analysis (QPA) of the thermal breakdown products of schorl.

Phase	Space group	*a* (Å)	*b* (Å)	*c* (Å)	*V* (Å^3)	wt%
B-Mullite	*Pbam*	7.5307(5)	7.6703(6)	2.8427(2)	164.20(2)	64.0(6)
Hematite	*R*-3*c*	5.02610(9)	= *a*	13.7084(3)	299.904(13)	26.9(5)
Tourmaline after HT	*R*3*m*	15.8577(14)	= *a*	7.2115(9)	1570.5(3)	9.2(3)
Pristine schorl	*R*3*m*	16.0050(3)	= *a*	7.1910(2)	1595.26(7)	100

atoms per formula unit (*apfu*) at the *T* site (Ballirano et al., 2022a).

Thermal expansion

The dependence of the studied schorl cell parameters from *T* is reported in Table 6, and their relative expansion as a function of *T* is shown in Figure 4.

The trend of the studied schorl is very similar to that observed in Fe-rich fluor-elbaite (Celata et al., 2021), Mn-bearing fluor-elbaite (Ballirano et al., 2022a) and uvite (Ballirano et al., 2022b) (Figure 5). The main event is evidenced by the significant contraction of the unit-cell parameters occurring, approximately, in the 450-675 °C thermal range. However, this contraction is more pronounced for schorl, consistently with the larger TE content as compared to that of the other tourmaline samples (schorl: 2.58 apfu Fe^{2+}; Fe-rich fluor-elbaite: 0.94 apfu Fe^{2+}+0.18 apfu Mn^{2+}; uvite: 0.47 apfu Fe^{2+}; Mn-bearing fluor-elbaite: 0.12 apfu Mn^{2+}). Based on reference data, the contraction is produced by the onset of the TE oxidation process, coupled to deprotonation at H1 and/or H3 sites. In the case of schorl the general equation describing the process takes the form of $(Fe^{2+})+(OH)^- \rightarrow (Fe^{3+})+(O^{2-})+1/2H_2(g)$, (Bosi et al., 2019). The thermal range for the onset of the coupled dehydrogenation-oxidation process converges with those observed in literature (e.g. Hovis et al., 2022; Pieczka and Kraczka, 2004; Castañeda et al., 2006; McKeown, 2008; Bačik et al., 2011; Filip et al., 2012; Liu et al., 2019) and it was constrained at ca. 450 °C.

It is worth noting that, in the 550-625 °C thermal range, a significant peak broadening/splitting is observed. This phenomenon may be explained by the simultaneous strong contraction of the unit-cell parameters and the presence of some longitudinal thermal gradient (Table 6).

The variation of the unit-cell parameters with *T* was modelled up to 425 °C, i.e. before the onset of TE oxidation, using the Berman equation (Berman 1988). Table 7 reports the relevant parameters of the fitting procedure. Data indicate that the *a*-parameter is softer than the *c*-parameter against *T*, coherently with other analyzed tourmalines. Uvite is, among those analyzed, the tourmaline showing the largest thermal expansion whereas elbaite minerals are characterized by smaller and very similar a_o and a_1 parameters. Schorl has an intermediate behavior (Figure 5 and Table 7). Our findings agree with Hoang et al. (2013), where variation of cell parameters, experienced before the breakdown, is correlated to the amount of TE (Fe^{2+} ions, and therefore to the oxidation of Fe^{2+} to Fe^{3+}).

The unit-cell parameters of the relict tourmaline recovered at R*T* after the heating run (Table 5) shows a significant contraction as compared to the pristine schorl, clearly indicating that the $(Fe^{2+})+(OH)^- \rightarrow (Fe^{3+})+(O^{2-})+1/2H_2(g)$ reaction has taken place and has been quenched to R*T*.

Unfortunately, the quality of the diffraction data prevents us from a detailed description of the structural modifications occurring during the heating run.

Unit-cell parameters of B-mullite and hematite during the thermal breakdown of schorl are reported in Table 8.

Schorl stability field

Referring to the diagram reported in van Hinsberg et al. (2011), the results obtained by our experimental work prove that schorl is still stable with respect to literature data (Holt and Johannes, 1991) when temperature approaches 825 °C and that breakdown is experienced between 825 and 850 °C. Schorl breakdown temperature at 3 Kbar from literature data is considerably lower, 750-775 °C (Holt and Johannes, 1991), mainly because it was analyzed in a SiO_2 saturated system in order to mimic a natural gneiss even if doped with an excess of tourmaline, and also because a certain water content (0.6 to 6.0 wt% H_2O) was added to the starting material.

CONCLUSIONS

The thermal behavior of schorl was investigated up to structural breakdown through *in situ* H*T*-pXRD. Results show higher breakdown temperature (~850 °C) with respect to the literature. Annealing the schorl at 450 °C in air was enough to set the Fe oxidation out, counterbalanced by the deprotonation reaction: $(Fe^{2+})+(OH)^- \rightarrow (Fe^{3+})+(O^{2-})+1/2H_2(g)$.

Tourmaline breakdown products were identified

Table 6. Refined unit-cell parameters of the studied schorl at the various temperatures.
In italics: thermal range where peak broadening/splitting was observed due to strong contraction of the unit-cell parameters and the presence of some longitudinal thermal gradient. * In mixture with B-mullite and hematite. Breakdown completed at 925 °C.

T (°C)	*a* (Å)	*c* (Å)	*V* (Å^3)	*wt% B-mullite*	*wt% hematite*
30	16.0050(3)	7.19099(15)	1595.26(7)	-	-
50	16.0057(3)	7.19236(15)	1595.70(7)	-	-
75	16.0079(3)	7.19435(15)	1596.57(7)	-	-
100	16.0091(3)	7.19564(15)	1597.11(7)	-	-
125	16.0110(3)	7.19794(15)	1597.99(7)	-	-
150	16.0129(3)	7.19980(15)	1598.80(7)	-	-
175	16.0143(3)	7.20142(16)	1599.43(7)	-	-
200	16.0165(3)	7.20364(15)	1600.35(7)	-	-
225	16.0181(3)	7.20577(15)	1601.14(7)	-	-
250	16.0201(3)	7.20787(15)	1602.02(7)	-	-
275	16.0224(3)	7.21013(16)	1602.98(7)	-	-
300	16.0242(3)	7.21226(17)	1603.82(7)	-	-
325	16.0260(3)	7.21442(18)	1604.65(8)	-	-
350	16.0287(3)	7.21713(17)	1605.81(8)	-	-
375	16.0309(3)	7.21963(18)	1606.79(8)	-	-
400	16.0322(3)	7.22168(17)	1607.51(8)	-	-
425	16.0350(3)	7.22434(17)	1608.68(8)	-	-
450	16.0363(4)	7.22664(19)	1609.44(9)	-	-
475	16.0367(4)	7.2284(2)	1609.91(9)	-	-
500	16.0368(5)	7.2307(2)	1610.45(11)	-	-
525	16.0365(5)	7.2327(3)	1610.83(12)	-	-
550	*16.0306(7)*	*7.2332(3)*	*1609.75(15)*	-	-
575	*16.0142(11)*	*7.2339(5)*	*1606.6(3)*	-	-
600	*15.9737(13)*	*7.2391(7)*	*1599.7(3)*	-	-
625	*15.9327(8)*	*7.2454(4)*	*1592.8(2)*	-	-
650	15.9180(4)	7.2528(2)	1591.51(10)	-	-
675	15.9150(4)	7.2587(2)	1592.23(10)	-	-
700	15.9176(3)	7.26292(18)	1593.66(8)	-	-
725	15.9180(3)	7.26553(18)	1594.38(8)	-	-
750	15.9208(3)	7.26905(19)	1595.65(8)	-	-
775	15.9227(3)	7.2734(2)	1596.98(8)	-	-
800	15.9236(4)	7.27787(19)	1598.15(8)	-	-
825	15.9255(3)	7.28344(18)	1599.76(7)	-	-
850*	15.9285(4)	7.28836(19)	1601.43(8)	-	2.3(2)
875*	15.9328(5)	7.2926(3)	1603.23(12)	26.0(3)	7.9(5)
900*	15.9314(15)	7.2914(9)	1602.7(4)	56.0(5)	12.1(11)
925	-	-	-	83.3(9)	16.7(9)

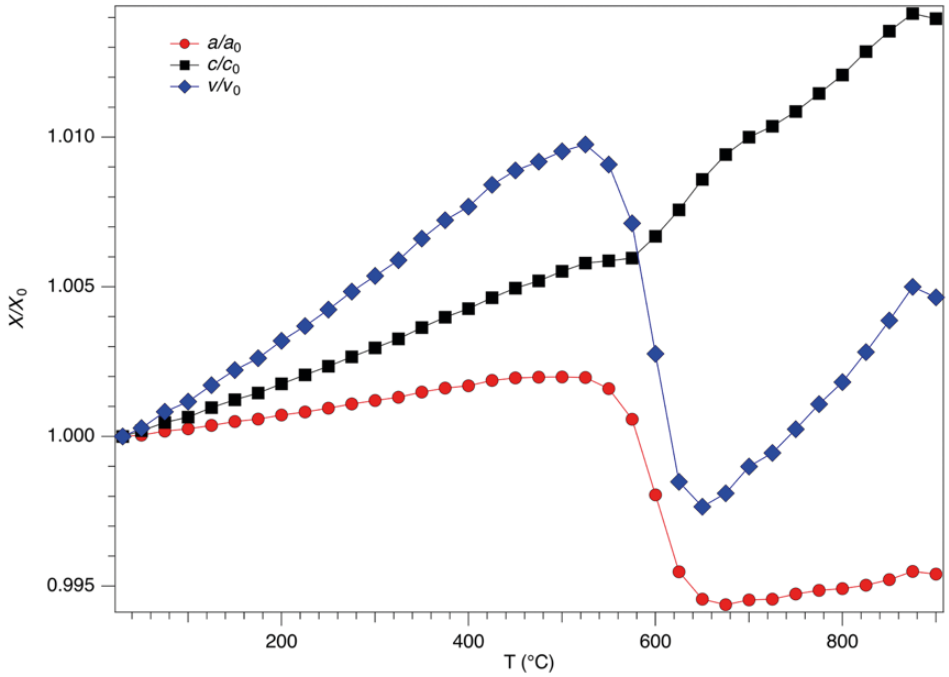

Figure 4. Variation of normalized unit-cell parameters with T for the schorl studied.

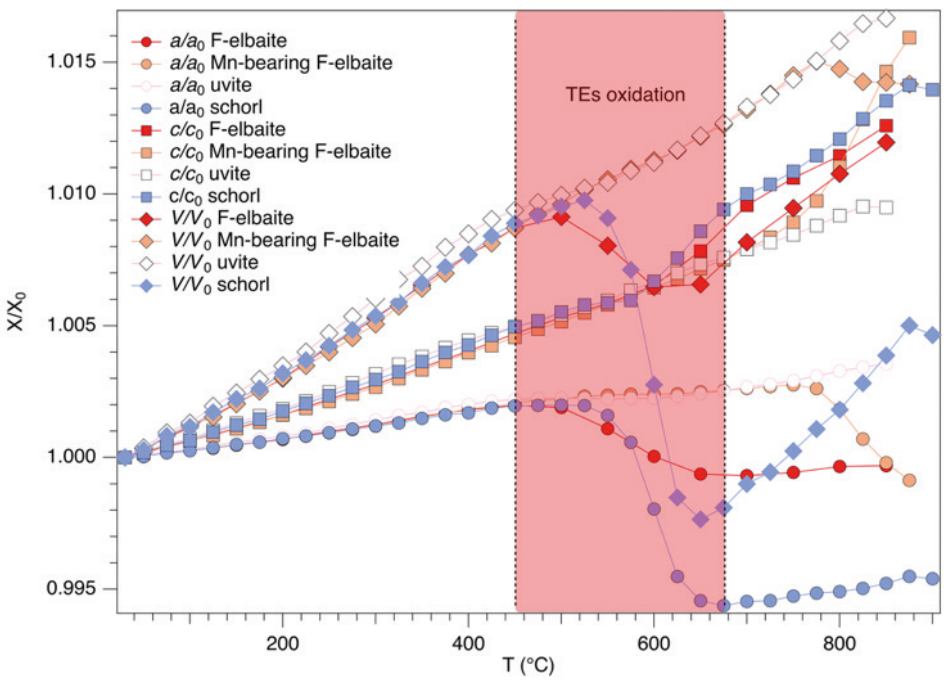

Figure 5. Comparison of the normalized unit-cell parameters from *T* for the various tourmaline species: schorl (present work), Fe-rich fluor-elbaite (Celata et al., 2021), Mn-bearing fluor-elbaite (Ballirano et al., 2022a), and uvite (Ballirano et al., 2022b).
The pinkish area delimitates the common temperature range where transition elements oxidation occurs.

Table 7. Relevant parameters of the fitting procedure by the Berman equation of the unit-cell parameters vs *T* data, up to oxidation, for different tourmaline species. Data of Fe-rich fluor-elbaite, Mn-bearing fluor-elbaite and uvite from Celata et al. (2021) and Ballirano et al. (2022 a,b).
Temperature of reference = 30 °C (303 K).
Uvite T_{max} 425 °C, step 25 °C;
Schorl T_{max} 425 °C, step 25 °C;
Fe-rich fluor-elbaite T_{max} 425 °C, step 50 °C;
Mn-bearing fluor-elbaite T_{max} 450 °C, step 25 °C;

		V_0, a_0, c_0 (Å^3, Å, Å)	a_0 (x 10^{-5} K^{-1})	a_1 (x 10^{-8} K^{-2})
V (Å^3)	Uvite	1597.54(8)	1.93(6)	2.1(3)
	Schorl	1595.22(5)	1.70(4)	2.19(19)
	Fe-rich fluor-elbaite	1564.38(6)	1.59(5)	2.6(3)
	Mn-bearing fluor-elbaite	1530.15(7)	1.56(5)	2.6(3)
a (Å)	Uvite	15.97420(23)	0.448(18)	0.55(9)
	Schorl	16.00479(19)	0.386(14)	0.46(7)
	Fe-rich fluor-elbaite	15.91875(19)	0.371(17)	0.66(10)
	Mn-bearing fluor-elbaite	15.7927(3)	0.36(2)	0.69(10)
c (Å)	Uvite	7.22912(17)	1.04(3)	0.97(15)
	Schorl	7.19103(10)	0.927(17)	1.28(8)
	Fe-rich fluor-elbaite	7.12842(8)	0.849(16)	1.32(9)
	Mn-bearing fluor-elbaite	7.08421(9)	0.841(16)	1.23(8)

Table 8. Unit-cell parameters of B-mullite and hematite during the thermal breakdown of schorl.

Phase	T (°C)	a (Å)	b (Å)	c (Å)	volume (Å^3)
B-Mullite	850	-	-	-	-
	875	7.579(4)	7.713(4)	2.8496(12)	166.56(14)
	900	7.571(2)	7.721(3)	2.8506(8)	166.62(9)
	925	7.5652(19)	7.730(2)	2.8504(7)	166.69(7)
Hematite	850	5.0740(12)	= a	13.819(5)	308.10(19)
	875	5.0801(3)	= a	13.8265(14)	309.02(5)
	900	5.0826(3)	= a	13.8349(11)	309.52(4)
	925	5.0827(3)	= a	13.8363(10)	309.56(5)

as a "boron-mullite" phase (dominant), and hematite plus some amorphous material and the breakdown reaction of schorl can be expressed as follows: $2NaFe^{2+}{}_3Al_6(BO_3)_3Si_6O_{18}(OH)=3Fe_2O_3+4/3Al_9Si_2BO_{19}$ +(Na- Si- B-rich) glass+$4H_2O$.

ACKNOWLEDGEMENTS

We acknowledge W. David Sinclair (emeritus, Geological Survey of Canada) for collecting the sample material.

Funding by Sapienza University of Rome grant (Prog. Università 2020) is acknowledged together with Ministero dell'Università e della Ricerca through the project PRIN 2020

"HYDROX - HYDRous- vs OXo-components in minerals: adding new pieces to the Earth's H2O cycle puzzle", prot. 2020WYL4NY.

REFERENCES

Andreozzi G.B., Bosi F., Celata B., Capizzi L.S., Stagno V., Beckett-Brown C., 2020. Crystal-chemical behavior of Fe^{2+} in tourmaline dictated by structural stability: insights from a schorl with formula $Na^{Y}(Fe^{2+}{}_2Al)^{Z}(Al_5Fe^{2+})(Si_6O_{18})(BO_3)_3(OH)_3(OH,F)$ from Seagull batholith (Yukon Territory, Canada). Physics and Chemistry of Minerals 47, 3-9.

Bačik P., Ozdín D., Miglierini M., Kardošová P., Pentrák M., Haloda J., 2011. Crystallochemical effects on heat treatment on Fe-dominant tourmalines from Dolní Bory (Czech Republic) and Vlachovo (Slovakia). Physics and Chemistry of Minerals 38, 599-611.

Ballirano P., 2003. Effects of the choice of different ionization level for scattering curves and correction for small preferred orientation in Rietveld refinement: the $MgAl_2O_4$ test case. Journal of Applied Crystallography 36, 1056-1061.

Ballirano P., Celata B., Skogby H., Andreozzi G.B., Bosi F., 2022a. H*T* breakdown of Mn-bearing elbaite from the Anjanabonoina pegmatite, Madagascar. Journal of Geosciences 67, 1-11. doi: 10.3190/jgeosci.347.

Ballirano P., Celata B., Bosi F., 2022b. In-situ high-temperature behaviour and breakdown conditions of uvite at room pressure. Physics and Chemistry of Minerals, in press.

Ballirano P. and Maras A., 2006. In-situ X-ray transmission powder diffraction study of the kinetics of the light induced alteration of realgar (α-As_4S_4). European Journal of Mineralogy 18, 589-599.

Ballirano P. and Melis E., 2007. Thermal behaviour of β-anhydrite $CaSO_4$ to 1,263K. Physics and Chemistry of Minerals 34, 699-704.

Berman R.G., 1988. Internally-consistent thermodynamic data for minerals in the system Na_2O-K_2O-CaO-MgO-FeO-Fe_2O_3-Al_2O_3-SiO_2-TiO_2-H_2O-CO_2. Journal of Petrology 29, 445-522.

Bosi F., 2018. Tourmaline crystal chemistry. American Mineralogy 103, 298-306.

Bosi F., Andreozzi G.B., Federico M., Graziani G., Lucchesi S., 2005. Crystal chemistry of the elbaite-schorl series. American Mineralogy 90, 1784-1792.

Bosi F., Skogby H., Hålenius U., 2019. Thermally induced cation redistribution in fluor-elbaite and Fe-bearing tourmalines. Physics and Chemistry of Minerals 46, 371-383.

Bruker AXS, 2016. Topas V6: General profile and structure analysis software for powder diffraction data. Bruker AXS, Karlsruhe, Germany.

Castañeda C., Eeckhout S.G., da Costa G.M., Botelho N.F., De Grave E., 2006. Effect of heat treatment on tourmaline from Brazil. Physics and Chemistry of Minerals 33, 207-216.

Celata B., Ballirano P., Andreozzi G., Bosi F., 2021. In-situ high-temperature behaviour of fluor-elbaite: breakdown conditions and products. Physics and Chemistry of Minerals 48, 24.

Cheary R.W. and Coelho A.A., 1992. A Fundamental Parameters Approach of X-ray line-profile fitting. Journal of Applied Crystallography 25, 109-121.

Dutrow B. and Henry D., 2011. Tourmaline: a geologic DVD. Elements 7, 301-306.

Filip J., Bosi F., Novàk M., Skogby H., Tuček J., Čuda J., Wildner M., 2012. Iron redox reactions in the tourmaline structure: High-temperature treatment of Fe^{3+}-rich schorl. Geochimica et Cosmochimica Acta 86, 239-256.

Hawthorne F.C., Ungaretti L., Oberti R., 1995. Site populations in minerals: terminology and presentation of results of crystal-structure refinement. Canadian Mineralogist 33, 907-911.

Henry D.J., Novák M., Hawthorne F.C., Ertl A., Dutrow B.L., Uher P., Pezzotta F., 2011. Nomenclature of the tourmaline supergroup minerals. American Mineralogist 96, 895-913.

Hoang L.H., Hien N.T.M., Chen X.-B., Yang I.S., 2013. Annealing effect in raman scattering of various types of tourmalines. Journal of Applied Spectroscopy 79, 881-887.

Holtz F. and Johannes W., 1991. Effect of tourmaline on melt fraction and composition of first melts in quartzofeldspathic gneiss. European Journal of Mineralogy 3, 527-536.

Liu X., Yu C., Yang W., Xie L., Liang S., 2019. Thermal decomposition kinetics of Fe-rich tourmaline. European Journal of Mineralogy 31, 919-928.

Lührs H., Soellradl S., King S.P., Hanna J.V., Konzett J., Fischer R.X., 2014. Ambient and high-pressure synthesis, composition, and crystal structure of B-mullites. Crystal Research Technology 49, 21-31.

McKeown D.A., 2008. Raman spectroscopy, vibrational analysis, and heating of buergerite tourmaline. Physics and Chemistry of Mineralogy 35, 259-270.

Pieczka A. and Kraczka J., 2004. Oxidized tourmalines: a combined chemical, XRD and Mossbauer study. European Journal of Mineralogy 16, 309-321.

Sabine T.M., Hunter B.A., Sabine W.R., Ball C.J., 1998. Analytical expressions for the transmission factor and peak shift in absorbing cylindrical specimens. Journal of Applied Crystallography 31, 47-51.

Sinclair W.D. and Richardson J.M., 1992. Quartz-tourmaline orbicules in the Seagull Batholith, Yukon Territory. Canadian Mineralogist 30, 923-935.

van Hinsberg V.J., Henry D.J., Marshall H.R., 2011. Tourmaline: An ideal indicator of its host environment. Canadian Mineralogist 49, 1-16.

Young R.A., 1993. Introduction to the Rietveld method: In: Young R.A. (Ed.) "The Rietveld method". Oxford University Press, 1-38.